

Dynamic analysis and DNA coding-based image encryption of memristor synapse-coupled hyperchaotic IN-HNN network

Shuang Zhao(赵双), Yunzhen Zhang(张云贞), Xiangjun Chen(陈湘军), Bin Gao(高彬), and Chengjie Chen(陈成杰)
Citation: Chin. Phys. B, 2026, 35 (**1**): 010502. DOI: 10.1088/1674-1056/ae1dec
http://cpb.iphy.ac.cn; http://iopscience.iop.org/cpb

What follows is a list of articles you may be interested in

Multi-scroll hopfield neural network excited by memristive self-synapses and its application in image encryption

Ting He(何婷), Fei Yu(余飞), Yue Lin(林越), Shaoqi He(何邵祁), Wei Yao(姚卫), Shuo Cai(蔡烁), and Jie jin(金杰)
Chin. Phys. B, 2025, 34 (**12**): 120506. DOI: 10.1088/1674-1056/adfeff

Coexisting and multiple scroll attractors in a Hopfield neural network with a controlled memristor

Qing-Qing Ma(马青青), An-Jiang Lu(陆安江), and Zhi Huang(黄智)
Chin. Phys. B, 2024, 33 (**12**): 120502. DOI: 10.1088/1674-1056/ad8148

Coexistence behavior of asymmetric attractors in hyperbolic-type memristive Hopfield neural network and its application in image encryption

Xiaoxia Li(李晓霞), Qianqian He(何倩倩), Tianyi Yu(余天意),Zhuang Cai(才壮), and Guizhi Xu(徐桂芝)
Chin. Phys. B, 2024, 33 (**3**): 030505. DOI: 10.1088/1674-1056/acf281

Design and FPGA implementation of a memristor-based multi-scroll hyperchaotic system

Sheng-Hao Jia(贾生浩), Yu-Xia Li(李玉霞), Qing-Yu Shi(石擎宇), and Xia Huang(黄霞)
Chin. Phys. B, 2022, 31 (**7**): 070505. DOI: 10.1088/1674-1056/ac4a71

FPGA implementation and image encryption application of a new PRNG based on a memristive Hopfield neural network with a special activation gradient

Fei Yu(余飞), Zinan Zhang(张梓楠), Hui Shen(沈辉), Yuanyuan Huang(黄园媛), Shuo Cai(蔡烁), and Sichun Du(杜四春)
Chin. Phys. B, 2022, 31 (**2**): 020505. DOI: 10.1088/1674-1056/ac3cb2

SPECIAL TOPIC — Biophysical circuits: Modeling & applications in neuroscience

Dynamic analysis and DNA coding-based image encryption of memristor synapse-coupled hyperchaotic IN-HNN network

Shuang Zhao(赵双)[1,2], Yunzhen Zhang(张云贞)[3], Xiangjun Chen(陈湘军)[1], Bin Gao(高彬)[4], and Chengjie Chen(陈成杰)[4,†]

[1] *School of Software and Big Data, Changzhou College of Information Technology, Changzhou* 213164, *China*
[2] *Department of Electrical Engineering, Faculty of Engineering, University of Malaya, Kuala Lumpur* 50603, *Malaysia*
[3] *School of Information Engineering, Xuchang University, Xuchang* 461000, *China*
[4] *School of Electrical and Information Engineering, Jiangsu University of Technology, Changzhou* 213001, *China*

(Received 10 September 2025; revised manuscript received 7 November 2025; accepted manuscript online 11 November 2025)

The rapid development of brain-like neural networks and secure data transmission technologies has placed greater demands on highly complex neural network systems and highly secure encryption methods. To this end, the paper proposes a novel high-dimensional memristor synapse-coupled hyperchaotic neural network by using the designed memristor as the synapse to connect an inertial neuron (IN) and a Hopfield neural network (HNN). By using numerical tools including bifurcation plots, phase plots, and basins of attraction, it is found that the dynamics of this system are closely related to the memristor coupling strength, self-connection synaptic weights, and inter-connection synaptic weights, and it can exhibit excellent hyperchaotic behaviors and coexisting multi-stable patterns. Through PSIM circuit simulations, the complex dynamics of the coupled IN-HNN system are verified. Furthermore, a DNA-encoded encryption algorithm is given, which utilizes generated hyperchaotic sequences to achieve encoding, operation, and decoding of DNA. The results show that this algorithm possesses strong robustness against statistical attacks, differential attacks, and noise interference, and can effectively resist known/selected plaintext attacks. This work will provide new ideas for the modeling of large-scale brain-like neural networks and high-security image encryption.

Keywords: inertial neuron (IN), Hopfield neural network (HNN), memristor synapse, hyperchaotic attractor, image encryption

PACS: 05.45.–a, 05.45.Pq

DOI: 10.1088/1674-1056/ae1dec **CSTR:** 32038.14.CPB.ae1dec

1. Introduction

In recent years, the use of coupled neural networks to simulate the dynamic processes of the brain has become the research frontier in the fields of artificial intelligence and neuromorphic computing.[1–3] The biological nervous system achieves advanced cognitive functions such as learning and memory through synaptic plasticity and neuronal dynamics. However, traditional artificial neural networks still have significant limitations in depicting such complex behaviors. For instance, the Hopfield neural network (HNN) possesses associative memory and optimization computing capabilities, but its performance is mostly confined to convergence or low chaotic states, making it difficult to reproduce the rich characteristics of biological neural networks.[4]

Artificial neurons and neural networks are the core components for constructing coupled neural networks. Among them, the inertial neuron (IN), as an important artificial neuron model, significantly expands the descriptive capabilities of traditional neuron models by introducing an inertial feedback mechanism, and can more accurately depict the dynamic characteristics of neurons. The IN model was first proposed by Babcock and Westervelt,[5] and later Wheeler and Schieve established a complete inertial neural network model based on this.[6] In recent years, with the introduction of new excitation mechanisms such as external alternating current stimulus[7] and bipolar pulse stimulus,[8] as well as the continuous expansion of the model structure,[9–13] significant progress has been made in the research of inertial neuron models, further enriching their application scenarios and theoretical value of the single IN model and the IN-based coupled network.

The memristor is widely regarded as an ideal synapse element for brain-like computing due to its non-volatile storage and dynamic conductance properties.[14–17] Its behavior closely aligns with the plasticity of biological synapses. Existing studies often adopt simplified coupling methods like electrochemical synapses, failing to fully utilize the nonlinear control capabilities of memristive synapses. In recent years, neural networks based on memristor synapses have demonstrated great potential in chaotic dynamics, associative memory, and image encryption applications.[18–20] For example,

†Corresponding author. E-mail: chengjiechen@jsut.edu.cn

© 2026 Chinese Physical Society and IOP Publishing Ltd. All rights, including for text and data mining, AI training, and similar technologies, are reserved.

Huang *et al.*[21] proposed a coupled HR-HNN model via a sine-type memristor, where coexisting attractors as well as attractor growing phenomenon were found. Biamou *et al.*[22] built a coupled HNN-HNN model via a multi-stable flux-controlled memristor, where coexisting bitstable patterns and double-bubbles bifurcation were confirmed. Sun *et al.*[23] presented a coupled HR-FN model by using a hyperbolic memristor. Based on numerical and circuit validation, tri-stable coexisting attractors have been demonstrated. Furthermore, a full-process DNA encryption algorithm has been made, which improves the security of data transmission. Furthermore, by connecting neurons through memristors, synchronous dynamics can also be discovered. For instance, Wang *et al.*[24] connected a discrete Chialvo neuron and a discrete Rulkov neuron through one locally active memristor and demonstrated that the intensity of synapse could induce phase synchronization of the neural network. Subsequently, Li *et al.*[25] constructed a nervous system using memristors to link HR neurons and revealed the phenomenon of remote synchronization driven by the memristor coupling strength. By introducing the memristor, the dynamics of neural networks can be further expanded, generating complex behaviors such as multistability, synchronization, and hyperchaos.[26–28]

Nonlinear dynamic systems can provide a rich set of chaotic sequences for encryption algorithms and are the foundation for building more highly secure cryptographic systems. Currently, common image encryption methods include classical algorithms based on the low-dimensional chaotic flow[29] and the group scrambling and diffusion method.[30] In recent years, DNA encryption algorithms have garnered widespread attention by combining the strengths of bioinformatics and chaos theory. Meng *et al.*[31] proposed a color image encryption algorithm based on a fractional-order five-dimensional hyperchaotic system, which extended the DNA encoding mechanism. Zhou *et al.*[32] proposed a multi-image encryption algorithm that combined a two-dimensional hyperchaotic model with DNA cyclic shift coding. This algorithm enhanced resistance to differential attacks through global permutation and multi-directional DNA diffusion driven by chaotic sequences. Then, they proposed a multi-image encryption algorithm that combines DNA coding with orthogonal arrays, achieving multi-threaded and bit-level encryption, significantly improving encryption efficiency and processing performance.[33]

Currently, the research scope of neural network dynamics is continuously expanding, ranging from basic phenomena such as aperiodic oscillations[3] and bifurcation[15] to complex behaviors such as bias control[20] and coexisting attractors.[27] As research progresses, these newly discovered dynamical phenomena are gradually being applied to various fields. Despite these advancements, the existing encryption schemes based on memristor-coupled neural networks usually rely on the generated chaotic sequences, which may have limitations in terms of complexity and randomness. However, the inertial neuron with simple mathematical expressions and complex dynamical behaviors has rarely been explored in the coupling networks. Constructing its coupling neural network models not only enables the simulation of more complex brain-like dynamics but also has the potential to generate hyperchaotic signals with high security features, thereby providing a new path for enhancing encryption security.

Therefore, this paper presents a novel memristor synapse-coupled hyperchaotic IN-HNN network to explore its nonlinear dynamics and the application in image encryption. The main contributions of this paper are threefold: (1) Construct a new mathematical model of a flux-controlled memristor with ReLU function and use it to couple the IN and HNN. Thus, a brain-like coupled neural network model can be established. (2) Reveal the complex hyperchaotic behavior related to the network parameters, as well as the coexistence of multi-stable states based on the initial values of neurons. (3) Design the DNA encoding strategy based on complex hyperchaotic sequences to enhance the security of image encryption. And the feasibility of the model and the robustness of the encryption algorithm are tested effectively.

The structure of this paper is as follows. Section 2 introduces the mathematical model of the memristor-coupled IN-HNN network. Section 3 explores the hyperchaotic and multi-stable behaviors of the coupled system. Section 4 presents circuit simulation results to verify the feasibility of the model. Section 5 injects a DNA encryption algorithm to realize the color image encryption. Section 6 summarizes the paper.

2. Memristor synapse-coupled IN-HNN model

This section first designs a new memristor system based on the ReLU function and depicts its pinched hysteresis loops. Then, the novel memristor is taken to couple the IN and HNN to construct a neural network.

2.1. A novel memristor model with ReLU function

The ReLU function is a nonlinear function with two segments, which is usually defined as $\mathrm{ReLU}(x) = \max(0, x)$. It can be used as an activation function[34–36] and has also been proven to be suitable for constructing a memristor model as a memductance function.[37–40] When the improved ReLU function is used as the memductance function, a new type of ReLU-based memristor system is proposed, and its constitutive relationship can be denoted as

$$\begin{cases} i = (\mathrm{ReLU}(\varphi) - \varphi)V, \\ \dot{\varphi} = V - \varphi, \end{cases} \tag{1}$$

where i, V, φ mean the output current, input voltage, and variables of the novel memristor, respectively. In addition, the

memductance function is denoted as $W(\varphi) = \mathrm{ReLU}(\varphi) - \varphi$. It is noted that both equations in Eq. (1) are dimensionless.

In order to prove the pinched hysteresis loops of the new memristor system, a sinusoidal voltage source $v = A\sin(2\pi ft)$ is supplied. Firstly, the initial value of the state variable $\varphi(0)$ is set as 0 all the time. Then, when $f = 1$ is assigned and A is set as 2, 3, 4, and 5 respectively, the voltage–current loci are plotted in Fig. 1(a). Besides, when $A = 3$ is given and f is set as 0.5, 1, 1.5, and 2 respectively, the simulated voltage–current loci are plotted in Fig. 1(b). As can be seen from Fig. 1, the pinched hysteresis loop satisfies three characteristic fingerprints of the memristor.

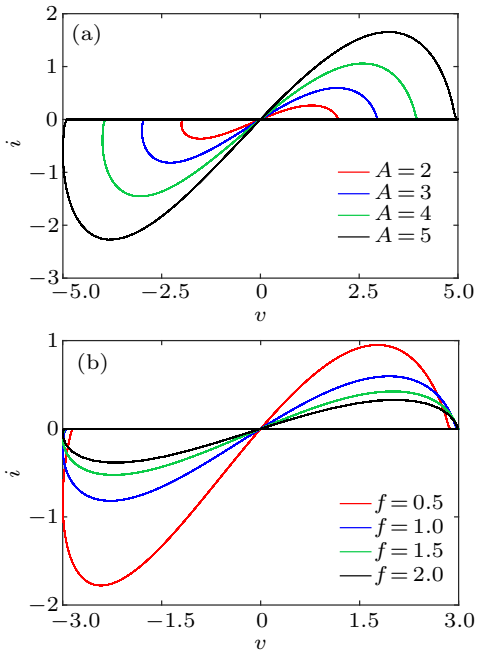


Fig. 1. The simulated pinched hysteresis loops of the ReLU function-based memristor system (1) under initial value $\varphi(0) = 0$: (a) $f = 1$ with different A. (b) $A = 3$ with different f.

2.2. Mathematical model of IN-HNN model

When the IN neuron is injected by the bipolar pulse current, a 2D improved IN model can be established.[8] In addition, a tri-neuron HNN model with a 3×3 synaptic weight matrix can be given, with the known weight matrix. Therefore, by using the proposed memristor as the coupler, a memristive IN-HNN network is built herein, and the equation of the coupled network model is written as

$$\begin{cases} \dot{x} = y + k(\mathrm{ReLU}(w) - w)(u - x), \\ \dot{y} = -y - 1.8x + 3.5\tanh(x) + 2\mathrm{sgn}(\sin(0.4\pi t)), \\ \dot{z} = -z + w_{11}\tanh(z) - 1.6\tanh(u) + w_{13}\tanh(v), \\ \dot{u} = -u + w_{21}\tanh(z) + w_{23}\tanh(v) \\ \qquad - k(\mathrm{ReLU}(w) - w)(u - x), \\ \dot{v} = -v - 100\tanh(z) + 0.5\tanh(u), \\ \dot{w} = u - x - w, \end{cases} \tag{2}$$

where k is the memristor coupling strength, w_{11} represents the self-connection synaptic weight and w_{13}, w_{21}, w_{23} are interconnection synaptic weights of the HNN model. In addition, in order to describe the structure of the coupling network in an intuitive way, the schematic diagram of the coupled IN-HNN network architecture is shown in Fig. 2.

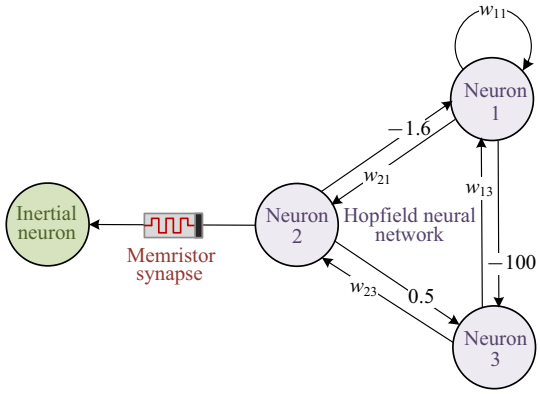


Fig. 2. Topology diagram of the coupled IN-HNN network through a memristive synapse.

As can be seen in Fig. 2, memristor synapses, IN, and HNN are taken as components, and they are integrated as a network. In Eq. (2), the variables z, u, and v are respectively represented by neurons 1, 2, and 3. Additionally, the membrane potential u of neuron 2 in HNN connects to the membrane potential x of the IN neuron through a memristor synapse. The synaptic weight parameters w_{11}, w_{13}, w_{21}, w_{23} are used to quantify the uncertain strengths between neurons. Note that the classical parameter values of the parameter are $w_{11} = 3.4$, $w_{13} = 0.7$, $w_{21} = 2.5$, and $w_{23} = 0.95$.

3. Complex dynamics analysis

This section reveals the dynamic behaviors for the coupled IN-HNN network, including memristor coupling strength-associated chaotic dynamics, synaptic weight-associated hyperchaos attractors, and initial value-associated coexistence behaviors.

3.1. Memristor coupled strength-associated chaotic dynamics

Firstly, taking k as the adjustable parameter, the influence on the dynamics of the coupling system is investigated. Numerical simulations are conducted using Lyapunov exponent spectra, bifurcation diagrams, and phase plots. With the fixed initial values (3, 0, 1, 0, 0, -1), the computation results are shown in Fig. 3.

The bifurcation diagram in Fig. 3(a) reveals the variation in the system state as k varies. The corresponding Lyapunov exponents quantitatively characterize the chaotic and periodic characteristics of the system under these parameters. Specifically, the coupled system is triggered by chaotic behavior. When $k = 0.474$, it enters the period-4 state, then jumps into the chaotic interval at $k = 0.942$, subsequently enters into a larger periodic region $k = [3.114, 3.810]$. Within this region,

multiple periodic bubbles appear, and the system alternates between multiple periods and chaotic intervals, eventually entering a large-scale chaotic interval. Figure 3(b) shows the phase plots generated under four specific k values. These phase plots visually demonstrate the attractor patterns at different k values, including the period-4 behavior at $k = 0.7$, the chaotic state at $k = 2$, the period-5 behavior at $k = 3.7$, and the multi-period state at $k = 8$.

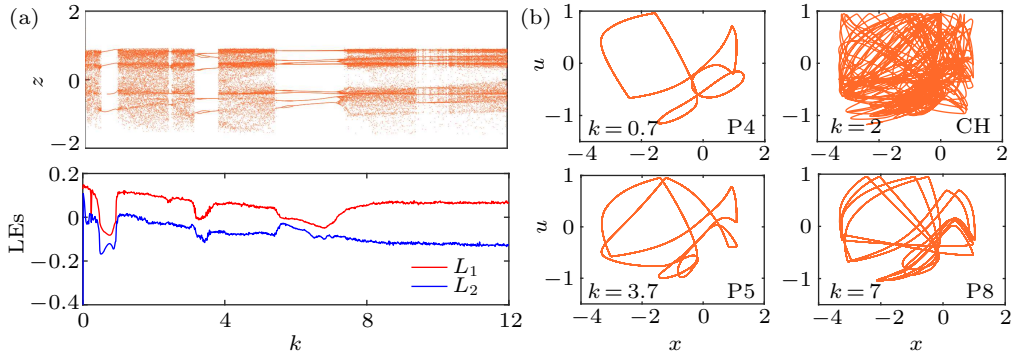


Fig. 3. Chaotic dynamics confirmed by bifurcation plots and phase plot with parameter k under $w_{11} = 3.4$, $w_{13} = 0.7$, $w_{21} = 2.5$, $w_{23} = 0.95$, and initial values (3, 0, 1, 0, 0, −1). (a) The k-dependent bifurcation diagram and Lyapunov exponents. (b) Phase plots with $k = 0.7$, $k = 2$, $k = 3.7$, $k = 7$.

3.2. Synaptic weight-associated hyperchaos attractors

Furthermore, the dynamics of partial synaptic connection weights under the condition of fixed memristor coupling strength and partial synaptic weights are investigated, and the numerical results are drawn in Figs. 4 and 5 systematically. Similarly, all simulations are conducted based on the initial values (3, 0, 1, 0, 0, −1).

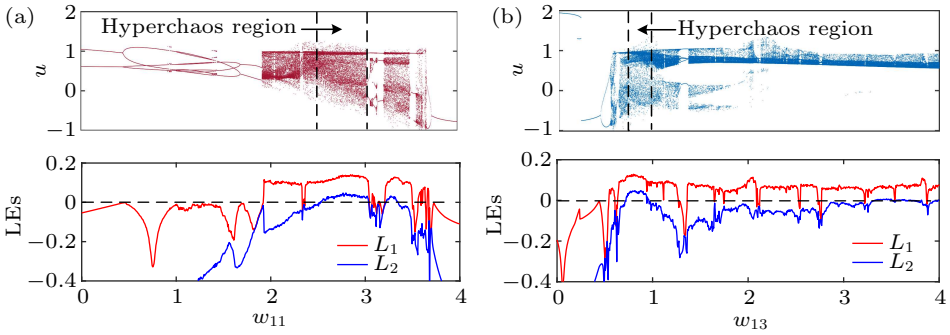


Fig. 4. Bifurcation behaviors simulated by using bifurcation plots and Lyapunov exponent spectra with adjustable synaptic weight parameters. (a) Bifurcation plots associated with parameter w_{11} under $k = 2$, $w_{13} = 0.7$, $w_{21} = 2.5$, $w_{23} = 0.95$, and initial values (3, 0, 1, 0, 0, −1). (b) Bifurcation plots associated with parameter w_{13} under $k = 2$, $w_{11} = 3.4$, $w_{21} = 2.5$, $w_{23} = 0.95$, and initial values (3, 0, 1, 0, 0, −1).

Figure 4(a) shows the bifurcation plots results as the parameter w_{11} changes, revealing the path of the system transition from periodic to chaotic motion patterns. It is noted that in the interval $w_{11} = [0, 1.93]$, periodic bubbles can still be observed. Additionally, in the interval $w_{11} = [2.53, 3.035]$, both the first two Lyapunov exponents are greater than 0, indicating the emergence of hyperchaotic behaviors. Figure 4(b) shows the bifurcation diagram of the variable u as the parameter w_{13} changes, depicting the complex state transitions induced by the inter-synaptic weight parameters. In the interval $w_{13} = [0.72, 0.96]$, both the first two Lyapunov exponents are also greater than 0, indicating the emergence of hyperchaotic behavior with w_{13}. These two bifurcation diagrams jointly demonstrate that synaptic weights are the key parameters that drive the system to bifurcate and induce complex hyperchaotic phenomena.

In Figs. 4(a) and 4(b), four sets of typical parameters are assigned to simulate the phase plots, as shown in Fig. 5. Through this series of phase diagrams, the specific attractor shapes and states corresponding to different parameters are intuitively presented.

When $k = 2$, $w_{13} = 0.7$, $w_{21} = 2.5$, $w_{23} = 0.95$, and initial values (3, 0, 1, 0, 0, −1) are fixed, and w_{11} is set to 0.5, 2, 2.8, and 4 respectively, the phase trajectories of the coupled system are depicted in Fig. 5(a). The attractors form states of period-2, hyperchaos, chaos, and period-1, with different shapes and amplitudes. When $k = 2$, $w_{11} = 3.4$, $w_{21} = 2.5$, $w_{23} = 0.95$, and initial values (3, 0, 1, 0, 0, −1) are fixed, and w_{13} is set to 0.3, 0.5, 0.9, and 3 respectively, the phase trajectories of the system are depicted in Fig. 5(b). As can be seen, period-1, hyperchaos, period-2, and chaos appear, indicating the existence of complex hyperchaotic phenomena in the memristor synapse-coupled IN-HNN network under specific parameters.

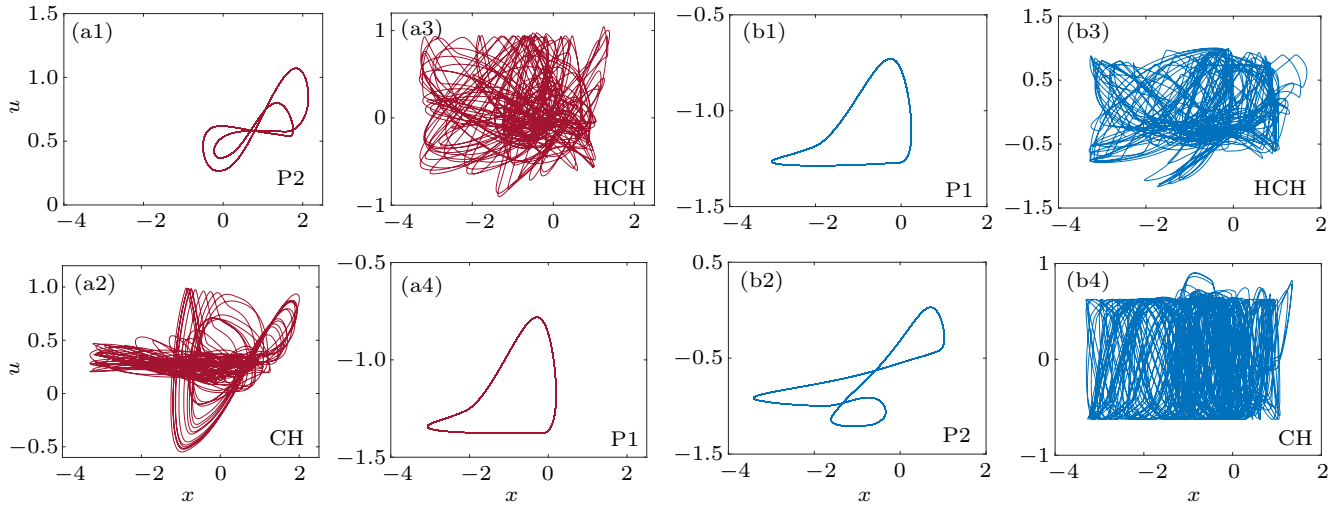


Fig. 5. Phase plots with assigned synaptic weight parameters: (a1) $w_{11} = 0.5$, (a2) $w_{11} = 2$, (a3) $w_{11} = 2.8$, (a4) $w_{11} = 4$, (b1) $w_{13} = 0.3$, (b2) $w_{13} = 0.5$, (b3) $w_{13} = 0.9$, (b4) $w_{13} = 3$.

3.3. Initial value-associated coexistence behaviors

The above research confirms that the parameter can trigger the emergence of complex dynamic behaviors, including bifurcation and hyperchaotic attractors. In fact, the initial values also have an effect on the network dynamics.

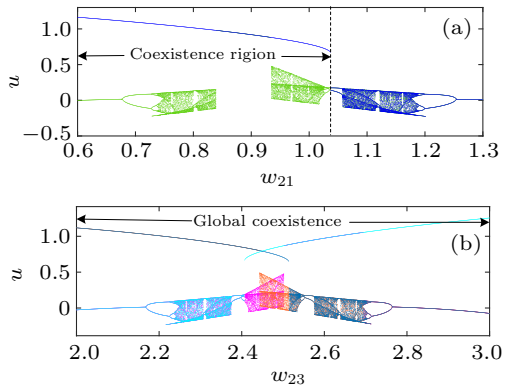


Fig. 6. Coexisting bifurcation behaviors associated with different initial values under adjustable parameters. (a) Parameters $k = 2$, $w_{11} = 3.4$, $w_{13} = 0.7$, $w_{23} = 0.95$ are fixed and initial values (3, 0, 1, 0, 0, 1) and (3, 0, 1, 0, 0, −1) are assigned. (b) Parameters $k = 2$, $w_{11} = 3.4$, $w_{13} = 0.7$, $w_{21} = 2.5$ are fixed and initial values (6, 0, 1, 0, 0, −1), (−6, 0, 1, 0, 0, −1), (3, 0, 1, 0, 0, −1), and (−3, 0, 1, 0, 0, −1) are assigned.

To illustrate the initial value effects, two examples based on the fixed parameter values are considered. First, when fixing the parameters $k = 2$, $w_{11} = 3.4$, $w_{13} = 0.7$, and $w_{23} = 0.95$, the coexisting bifurcation diagrams of the system (2) with respect to w_{21} for two sets of different initial values (3, 0, 1, 0, 0, 1) (green) and (3, 0, 1, 0, 0, −1) (blue) are depicted in Fig. 6(a). For the same parameter w_{21}, the system can evolve into two completely different routes, proving that there exist coexisting bi-stable attractors. Furthermore, when fixing the parameters $k = 2$, $w_{11} = 3.4$, $w_{13} = 0.7$, and $w_{21} = 2.5$, four bifurcation curves with w_{23} as the bifurcation parameter can be plotted in Fig. 6(b). These four curves are derived from four different initial conditions, namely, (6, 0, 1, 0, 0, −1) (sky blue), (−6, 0, 1, 0, 0, −1) (cyan), (3, 0, 1, 0, 0, −1) (bright purple), and (−3, 0, 1, 0, 0, −1) (orange). Such a complex bifurcation structure indicates that the system can simultaneously exist with four coexisting attractors globally, i.e., four-stable patterns under the regulation of the w_{23} parameter and initial values. This figure reveals the high sensitivity of the dynamic behaviors to the initial values.

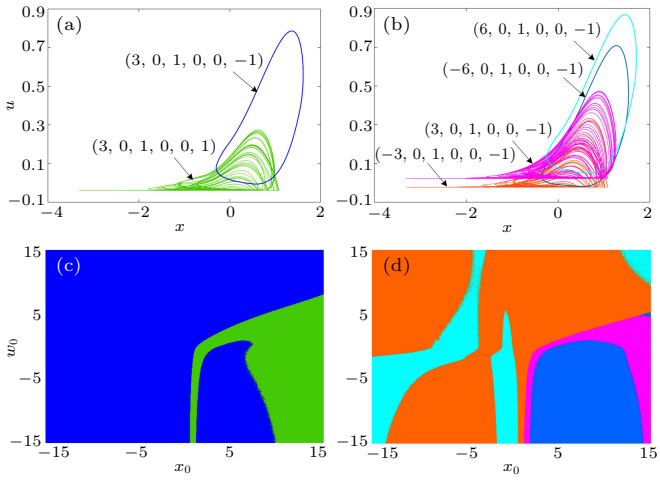


Fig. 7. Coexisting patterns simulated by phase plots as well as local attraction basins. (a) Coexisting phase plot under $k = 2$, $w_{11} = 3.4$, $w_{13} = 0.7$, $w_{23} = 0.95$, and initial values (3, 0, 1, 0, 0, 1) and (3, 0, 1, 0, 0, −1). (b) Coexisting phase plot under $k = 2$, $w_{11} = 3.4$, $w_{13} = 0.7$, $w_{21} = 2.5$, and initial values (6, 0, 1, 0, 0, −1), (−6, 0, 1, 0, 0, −1), (3, 0, 1, 0, 0, −1), and (−3, 0, 1, 0, 0, −1). (c) Local attraction basins under $k = 2$, $w_{11} = 3.4$, $w_{13} = 0.7$, $w_{23} = 0.95$, and initial values (x_0, 0, 1, 0, 0, w_0). (d) Local attraction basins under $k = 2$, $w_{11} = 3.4$, $w_{13} = 0.7$, $w_{21} = 2.5$, and initial values (x_0, 0, 1, 0, 0, w_0).

Further, under the fixed parameters, the multi-stability phenomena described by the attracting basin and coexistence phase plots are drawn, as shown in Fig. 7. When the parameter is set as $w_{21} = 1$, two asymmetric attractors induced by two different initial values exist simultaneously in the phase plots, which exhibit coexistence of the periodic and chaotic attractors. When the parameter is set as $w_{23} = 2.5$, four asym-

metric attractors induced by four different initial values exist simultaneously in the phase plots also, including two period-1 attractors and two period-2 chaotic attractors.

Figures 7(c) and 7(d) correspond to the initial plane under the parameter conditions of Figs. 7(a) and 7(b). In detail, Fig. 7(c) depicts the attractor domain for two types of attractors in the plane x_0–w_0. The blue color represents the period-1 state and the green color represents the chaotic behavior. It clearly shows the distribution of the regions for two coexisting attractors. Moreover, Fig. 7(d) shows four types of attractor domain structure under the parameter settings. Its shape is usually more complex, and the sky blue, cyan, bright purple, and orange colors represent upper period-1, lower period-1, upper chaos, and lower chaos, respectively. Therefore, the initial value affects the dependence of the multistable behavior in the coupled network.

4. PSIM circuit simulations

The memristor synapse-coupled IN-HNN model (2) can be developed by the equivalent analog circuit, as depicted in Fig. 8. Therein, we integrate six integral channels to form a complete main circuit. By using operational amplifiers, capacitors, resistors, multipliers, and other modules, the analog circuit for the coupled neural network is successfully realized.

In Fig. 8, $v_{\rm a}$, $v_{\rm b}$, and $v_{\rm c}$ are the output node voltages of three tanh modules, and their values are $-\tanh(V_z)$, $-\tanh(V_u)$, and $-\tanh(V_v)$, respectively. Furthermore, the node A is the output voltage terminal of the memristor, and the corresponding value is $(\mathrm{ReLU}(V_w)-V_w)(V_u-V_x)$. Based on the equivalent circuit, the circuit equations corresponding to model (2) can be built as

$$\begin{cases} RC\dfrac{\mathrm{d}V_x}{\mathrm{d}t} = V_y + \dfrac{R}{R_k}(\mathrm{ReLU}(V_w)-V_w)(V_u-V_x), \\ RC\dfrac{\mathrm{d}V_y}{\mathrm{d}t} = -V_y - \dfrac{R}{R_1}V_x + \dfrac{R}{R_2}\tanh(V_x) \\ \qquad\qquad + \dfrac{R}{R_3}\mathrm{sgn}\left(\sin(0.4\pi t)\right), \\ RC\dfrac{\mathrm{d}V_z}{\mathrm{d}t} = -V_z + \dfrac{R}{R_4}\tanh(V_z) \\ \qquad\qquad - \dfrac{R}{R_5}\tanh(V_u) + \dfrac{R}{R_6}\tanh(V_v), \\ RC\dfrac{\mathrm{d}V_u}{\mathrm{d}t} = -V_u + \dfrac{R}{R_7}\tanh(V_z) + \dfrac{R}{R_8}\tanh(V_v) \\ \qquad\qquad - \dfrac{R}{R_k}(\mathrm{ReLU}(V_w)-V_w)(V_u-V_x), \\ RC\dfrac{\mathrm{d}V_v}{\mathrm{d}t} = -V_v - \dfrac{R}{R_9}\tanh(V_z) + \dfrac{R}{R_{10}}\tanh(V_u), \\ RC\dfrac{\mathrm{d}V_w}{\mathrm{d}t} = V_u - V_x - V_w. \end{cases} \tag{3}$$

Herein, the integration time constant in Eq. (3) is set to $RC = 0.1$ ms ($R = 10$ kΩ and $C = 10$ nF). Corresponding to the mathematical Eq. (2) with classical parameter settings, the resistances in Eq. (3) can be derived as $R_k = R/2 = 5$ kΩ, $R_1 = R/1.8 = 5.556$ kΩ, $R_2 = R/3.5 = 2.857$ kΩ, $R_3 = R/2 = 5$ kΩ, $R_4 = R/3.4 = 2.941$ kΩ, $R_5 = R/1.6 = 6.25$ kΩ, $R_6 = R/0.7 = 14.286$ kΩ, $R_7 = R/2.5 = 4$ kΩ, $R_8 = R/0.95 = 10.526$ kΩ, $R_9 = R/100 = 0.1$ kΩ, and $R_{10} = R/0.5 = 20$ kΩ.

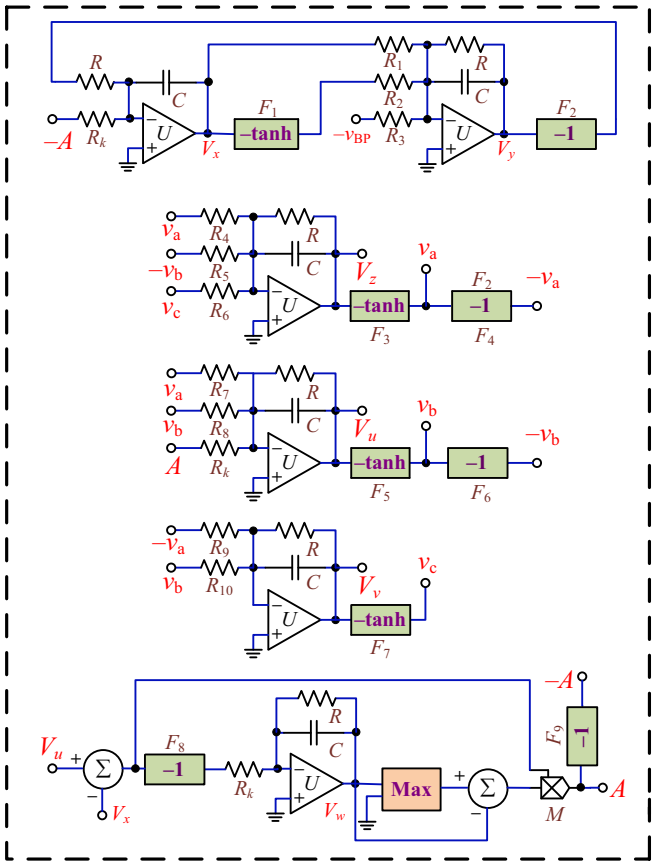


Fig. 8. The circuit diagram for implementing the memristor synapse-coupled IN-HNN model.

The coupled IN-HNN network circuit is developed in the PSIM software. When other values are kept constant, and R_4 is set to 20 kΩ, 5 kΩ, 3.571 kΩ, and 2.5 kΩ respectively, the circuit simulations are captured and depicted in Fig. 9(a). The phase diagram of the circuit exhibits different dynamic behaviors, including period-2, hyperchaos, chaos, and period-1 behaviors. Additionally, when the typical parameters remain unchanged, and R_6 is set to 33.333 kΩ, 20 kΩ, 11.111 kΩ, and 3.333 kΩ respectively, the circuit simulations are saved and depicted in Fig. 9(b). The phase diagram of the circuit exhibits period-1, hyperchaos, period-2, and chaos.

It is noted that the initial voltages of six capacitors are set to (3 V, 0 V, 1 V, 0 V, 0 V, −1 V) all the time. Thus, the circuit simulations are consistent with the numerical results in Fig. 5, effectively confirming the realizability of the presented model.

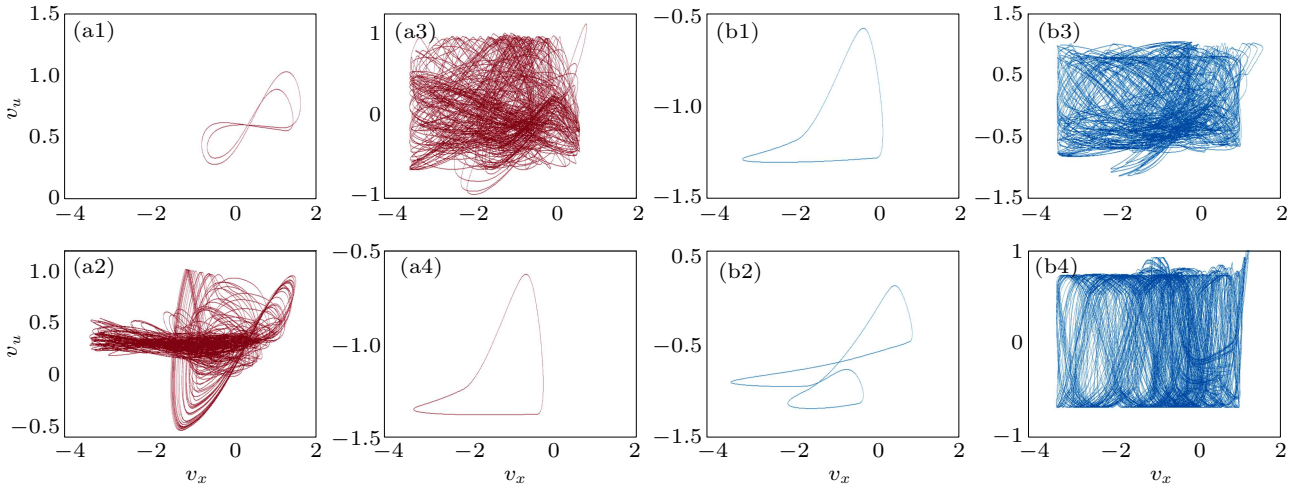


Fig. 9. Phase diagrams with assigned resistance values: (a1) $R_4 = 20$ kΩ, (a2) $R_4 = 5$ kΩ, (a3) $R_4 = 3.571$ kΩ, (a4) $R_4 = 2.5$ kΩ, (b1) $R_6 = 33.333$ kΩ, (b2) $R_6 = 20$ kΩ, (b3) $R_6 = 11.111$ kΩ, (b4) $R_6 = 3.333$ kΩ.

5. DNA coding-based color image encryption

Nowadays, digital image encryption technology based on chaos has various applications.[41] Fortunately, the memristor coupling network proposed in this paper can generate complex hyper-chaotic attractors by adjusting parameters. Based on this, this section further designs a DNA-encoded encryption algorithm, significantly enhancing the security of image encryption.

5.1. NIST test

Before applying the image encryption process, the proposed chaotic system is first evaluated for randomness. PRNG is a useful way for generating random sequences in a nonlinear dynamic system. Each of its numbers is completely determined by an initial value and is a basic application in secure communications. Based on the memristive IN-HNN model, four chaotic sequences are extracted, and the parameters of the sequences are shown in Table 1 below. In addition, the digits from the 38th to the 45th bit are extracted for random testing.

This test is conducted using NIST SP800-22 standard. MATLAB software was used to generate binary sequences with 5.0×10^6 rows and 4.5×10^7 characters. The randomness of sequences is tested by using Cygwin software. The number of byte streams in the test was set to 76. Table 1 lists the measured values generated under four different parameters. The four sequences tested are chaotic sequences used in image encryption. The results show that all obtained p-values exceed the significance level of 0.01, indicating that the random sequences exhibit satisfactory randomness properties and are suitable for image encryption applications.

Table 1. NIST test results of four random sequences with different parameters.

No.	Sub-tests	PRNGs				Result
		$(w_{11} = 2.8, w_{13} = 0.7)$	$(w_{11} = 2.8, w_{13} = 0.7)$	$(w_{11} = 3.4, w_{13} = 0.9)$	$(w_{11} = 3.4, w_{13} = 0.9)$	
		p-value$_x$	p-value$_u$	p-value$_x$	p-value$_u$	
01	Frequency	0.398690	0.821681	0.711017	0.144153	> 0.01
02	Block frequency	0.651990	0.424193	0.182977	0.327854	> 0.01
03	CumulativeSums (F)	0.266044	0.739918	0.247472	0.969690	> 0.01
	CumulativeSums (R)	0.055866	0.144153	0.622249	0.026435	> 0.01
04	Runs	0.350485	0.229900	0.622249	0.182977	> 0.01
05	Longest runs	0.087086	0.768138	0.534146	0.944860	> 0.01
06	Rank	0.592591	0.450564	0.374107	0.247472	> 0.01
07	FFT	0.505629	0.266044	0.213309	0.398690	> 0.01
08	Non-Ovla. Temp.	0.445255	0.388306	0.386823	0.366070	> 0.01
09	Ovla. Temp.	0.055866	0.821681	0.014777	0.213309	> 0.01
10	Universal	0.978900	0.891622	0.651990	0.681642	> 0.01
11	Appr. entropy	0.929192	0.768138	0.739918	0.651990	> 0.01
12	Ran. Exc.	0.315830	0.373997	0.646059	0.291075	> 0.01
13	Ran. Exc. Var.	0.207508	0.231585	0.527186	0.301621	> 0.01
14	Serial_1	0.035174	0.374107	0.622249	0.306232	> 0.01
	Serial_2	0.534146	0.450564	0.266044	0.197677	> 0.01
15	Linear complexity	0.182977	0.795464	0.505629	0.014695	> 0.01

5.2. Image encryption algorithm using DNA coding

The proposed algorithm presents an image encryption framework that integrates random sequences and DNA coding rules. By modifying pixel values through an unpredictable encryption mechanism, the algorithm ensures that the cipher image exhibits strong randomness, thereby enhancing the security of image information. The overall procedure consists of four major stages, including image preprocessing, chaotic sequence generation, DNA encoding, and encryption operations. Specific steps are as follows.

Step 1 Read the original image $\boldsymbol{P}$ and divide it into $\boldsymbol{P}_1$, $\boldsymbol{P}_2$, and $\boldsymbol{P}_3$ according to the channels of R, G, and B. Fill these three 2D matrices with zero values in order to the matrices all satisfy

$$\begin{cases} \mathrm{mod}\,(M,t)=0, \\ \mathrm{mod}\,(N,t)=0, \end{cases} \tag{4}$$

where t is the block size, and the image size after zero padding is defined as $M\times N$.

Step 2 Use the logistic map to generate the discrete chaotic sequence $\boldsymbol{L}_{1i}$. Set the value of parameter μ to 3.7. The initial value l_0 of the logistic map is calculated using Eq. (5). It represents the average grayscale of the pixels in the R and G channels of the image and can be used as the encryption key. The sequence $\boldsymbol{L}_{1i}$ is converted into a matrix $\boldsymbol{R}$ of size $M\times N$, with the matrix values ranging from [0, 255].

$$\begin{cases} l_{n+1}=\mu l_n(1-l_n), \\ l_0=\dfrac{\sum_{i=1,j=1}^{255}[P_1(i,j)+P_2(i,j)]}{M\times N\times 255\times 2}. \end{cases} \tag{5}$$

Step 3 Use the initial condition of the IN-INN model as the secret key to generate four hyperchaotic sequences $\boldsymbol{X}_i$, $\boldsymbol{Y}_i$, $\boldsymbol{Z}_i$, $\boldsymbol{K}_i$. The parameter matrices of $\boldsymbol{X}_i$ and $\boldsymbol{Y}_i$ are set according to formula (6), and the parameter matrices of $\boldsymbol{Z}_i$ and $\boldsymbol{K}_i$ are set according to formula (7).

$$\begin{bmatrix} w_{11} & w_{13} \\ w_{21} & w_{23} \end{bmatrix}=\begin{bmatrix} 2.8 & 0.7 \\ 2.5 & 0.95 \end{bmatrix}, \tag{6}$$

$$\begin{bmatrix} w_{11} & w_{13} \\ w_{21} & w_{23} \end{bmatrix}=\begin{bmatrix} 3.4 & 0.9 \\ 2.5 & 0.95 \end{bmatrix}. \tag{7}$$

Step 4 In DNA-based encoding, the four base pairs A, T, C, and G are mapped to binary pairs 00, 11, 10, and 01 following biological principles. Considering the Watson–Crick complementarity, only 8 possible encoding permutations are valid, as listed in Table 2.

Table 2. The eight admissible DNA coding rules.

Rules	1	2	3	4	5	6	7	8
11	T	T	C	C	G	G	A	A
01	G	C	A	T	A	T	G	C
10	C	G	T	A	T	A	C	G
00	A	A	G	G	C	C	T	T

Step 5 DNA operations are categorized into four types: addition, subtraction, exclusive-or, and exclusive-nor. Different encoding methods have different operation results. The specific operation rules adopted in this encryption algorithm are listed in Table 3.

Table 1. The four DNA arithmetic operations.

Base	ADD				SUB				XOR				XNOR			
	A	T	C	G	A	T	C	G	A	T	C	G	A	T	C	G
A	A	T	C	G	A	G	C	T	C	G	A	T	A	T	C	G
T	T	C	G	A	T	A	G	C	G	C	T	A	T	A	G	C
C	C	G	A	T	C	T	A	G	A	T	C	G	C	G	A	T
G	G	A	T	C	G	C	T	A	T	A	G	C	G	C	T	A

Step 6 Blocks at the same positions of $\boldsymbol{P}_1$, $\boldsymbol{P}_2$ and $\boldsymbol{P}_3$ are DNA-encoded using sequence $\boldsymbol{X}_i$. Sequence $\boldsymbol{Y}_i$ specifies the encoding rule of each sub-block in $\boldsymbol{R}$, while sequence $\boldsymbol{Z}_i$ defines the operation between matrices $\boldsymbol{P}_1$, $\boldsymbol{P}_2$, $\boldsymbol{P}_3$ and the corresponding block $\boldsymbol{R}$. The result of the operation is then combined with the previous block using the sequence number $\boldsymbol{Z}_i$ to enhance its diffusion. The sequences are finally converted to integers in the ranges [1, 8], [1, 8], and [0, 3], respectively.

Step 7 After the DNA operations, decoding is applied to the matrix blocks to obtain matrices $\boldsymbol{Q}_1$, $\boldsymbol{Q}_2$ and $\boldsymbol{Q}_3$. The sequence $\boldsymbol{K}_i$ specifies the decoding rules for each sub-block.

Step 8 Logistic map is then utilized to make two chaotic sequences $\boldsymbol{L}_{2i}$ and $\boldsymbol{L}_{3i}$, with parameter $\mu=3.7$. Their initial values are determined by the following formula:

$$\begin{cases} l_{01}=\dfrac{\sum_{i=1,j=1}^{255}[P_1(i,j)+P_3(i,j)]}{M\times N\times 255\times 2}, \\ l_{02}=\dfrac{\sum_{i=1,j=1}^{255}[P_2(i,j)+P_3(i,j)]}{M\times N\times 255\times 2}. \end{cases} \tag{8}$$

Step 9 Sort the sequences $\boldsymbol{L}_{2i}$ and $\boldsymbol{L}_{3i}$ in descending to generate the position sequences $\boldsymbol{H}_x$ and $\boldsymbol{H}_y$, recording the indices of elements before sorting. Use the position and index sequences to permute the rows and columns of $\boldsymbol{Q}_1$, $\boldsymbol{Q}_2$, and $\boldsymbol{Q}_3$, respectively. Combine the three permuted matrices into a 3D matrix yields the cipher image $\boldsymbol{Q}$.

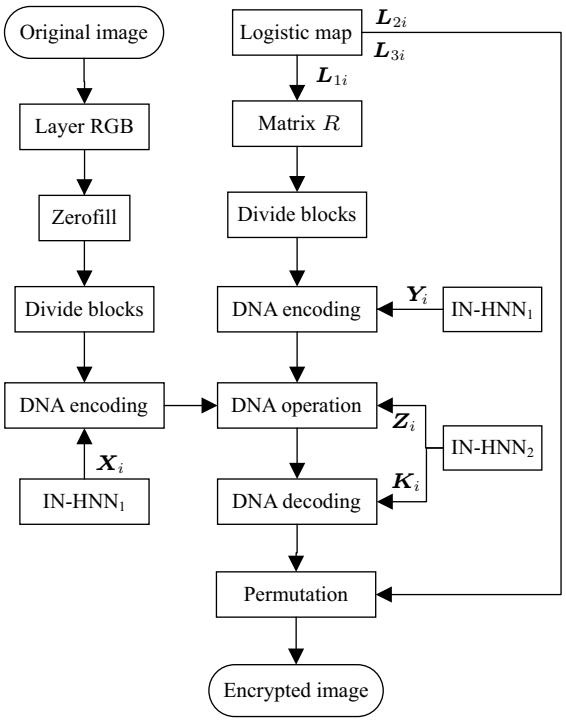


Fig. 10. Flowchart for DNA coding-based image encryption.

Based on the above algorithm process, a flowchart for image encryption is drawn in Fig. 10. It presents the key modules of the algorithm, allowing for a clearer view of the encryption process and facilitating the understanding of this DNA encryption algorithm.

To more clearly demonstrate the innovation and advantages of the algorithm proposed in this paper, a systematic comparison between the DNA encryption algorithm based on IN-HNN proposed in this paper and the existing typical DNA image encryption methods is deployed, as shown in Table 4. Compared with the traditional algorithms based on low-dimensional chaotic systems or fixed DNA rules, this method combines the high-dimensional hyperchaotic IN-HNN neural network with dynamic DNA encoding and multi-round diffusion mechanism, which can generate more complex chaotic sequences and achieve stronger diffusion and randomness. In addition, the algorithm demonstrates higher security in resisting known plaintext and chosen plaintext attacks, with a larger key space and an entropy value closer to the theoretical ideal value.

Table 4. Comparisons of the previous DNA encryption with this work.

Refs	Chaotic source	Dynamic behaviors	Key structure	DNA encoding method
[42]	4D ReLU-type local active memristor-based Hopfield neural network (MRHNN)	Chaos, offset boosting	Four initial values of the RHNN model	Fixed encoding and XOR operation
[43]	3D unified chaotic system	Chaos	The input of each stage together constitutes the runtime key	Dynamic encoding and multi-directional DNA scrambling
[32]	2D cross-coupling chaotic pattern (2D-CCP)	Hyperchaos	Plaintextrelated key	Cyclic shift DNA encoding algorithm
[44]	2D discrete memristive logistic map (2D-MLM)	Hyperchaos	Two parameters μ, k and two initial values of 2D-MLM, and four initial values of the multiwing hyperchaotic system	Blocked DNA encoding and diffusion driven by multiple pseudorandom sequences
This work	6D memristor synapse-coupled inertial neuron and Hopfield neural network model (IN-HNN)	Hyperchaos, coexistence behavior	Nine initial values of the IN-HNN system and three logistic discrete maps	Joint coding and multi-round diffusion mechanism of two sets of hyperchaotic sequences

5.3. Encryption performance analysis

To verify the reliability and security of the proposed encryption algorithm, a series of performance evaluations is conducted. The analysis focuses on three aspects: statistical characteristics, differential sensitivity, and robustness against common attacks. This study chose the MATLAB simulation platform for deployment and testing. Here, three images 4.2.01, 4.2.03 and 4.2.07 are taken as examples. In the established memristor IN-HNN model (2), the memristor parameter $k = 2$ is set, and the initial value is $(3,\ 0,\ 1,\ 0,\ 0,\ -1)$. Besides, the first set of parameters are $k = 2$, $w_{11} = 2.8$, $w_{13} = 0.7$, $w_{21} = 2.5$, and $w_{23} = 0.95$. The second set of parameters are $k = 2$, $w_{11} = 3.4$, $w_{13} = 0.9$, $w_{21} = 2.5$, and $w_{23} = 0.95$.

The value of parameter k directly determines the dynamic behaviors of the coupled IN-HNN system, which in turn affects the characteristics of the pseudo-random sequence used for encryption, and ultimately has a direct impact on the histogram distribution of the ciphertext image, the correlation between adjacent pixels, information entropy, NPCR/UACI, and robustness, etc. As can be seen in Fig. 3, when $k = 0.7$, 3.7, and 7, the IN-HNN system behaves as the periodic state, while $k = 2$ is assigned, the system takes on the chaotic state. At this time, the generated sequence has high unpredictability and is suitable for chaotic image encryption. In addition, the weight parameters w_{11}, w_{13}, w_{21}, and w_{23} can also induce bifurcation behaviors and produce complex dynamics. For example, when w_{11} is within the interval [2.53, 3.035], or when w_{13} is within the interval [0.72, 0.96], the IN-HNN system can exhibit hyperchaotic characteristics. Based on this property, the model has higher dimensions, better randomness, and stronger sensitivity to initial conditions, so the designed algorithm can effectively expand the key space of the system and significantly

enhance its ability to resist various attacks.

(1) Encryption/decryption and histogram analysis

The results of encryption, decryption and histogram analysis, are shown in Fig. 11. Figure 10(a) shows the original images, Fig. 11(c) shows the encrypted images and Fig. 11(e) shows the decrypted images. The results show that the algorithm can successfully encrypt color images, and the decrypted images are completely consistent with the original images, verifying the effectiveness of the encryption and decryption algorithm.

Figures 11(b) and 11(d) show the histograms of the original and encrypted images, respectively. The histograms of the three original images display nonuniform and irregular distributions. However, the histograms of the encrypted images demonstrate an approximately uniform distribution of pixel values, which confirms the strong security capability of the algorithm.

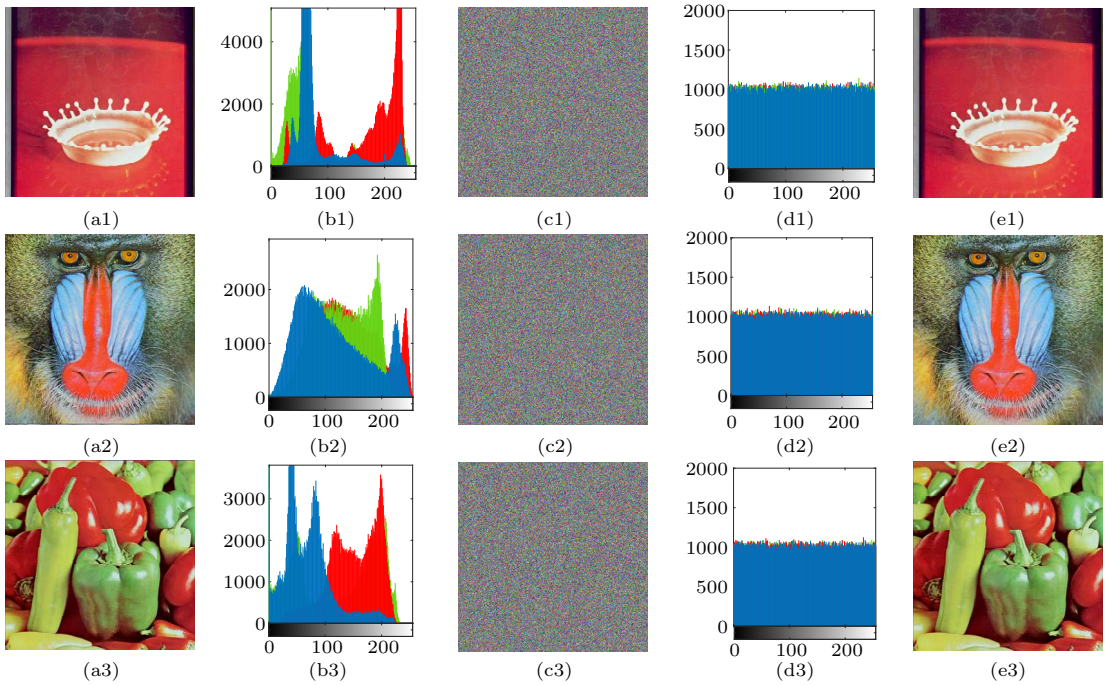


Fig. 11. Encryption/decryption and histogram. (a) Plain images. (b) Histograms of the plain images. (c) Encrypted images. (d) Histograms of the cipher images. (e) Decrypted images.

(2) Correlation coefficient and information entropy analysis

Correlation and entropy analysis are also important indicators for evaluating the encryption performance of algorithms. The correlation coefficient can be analyzed from three directions: horizontal, vertical, and diagonal. The ideal value of the correlation coefficient of the encrypted image is 0. The calculation formula is as follows:

$$\begin{cases} E(x) = \frac{1}{N}\sum_{i=1}^{N} x_i, \\ E(y) = \frac{1}{N}\sum_{i=1}^{N} y_i, \\ \mathrm{cov}(x,y) = \dfrac{\sum_{i=1}^{N}(x_i - E(x))(y_i - E(y))}{\sqrt{\sum_{i=1}^{N}(x_i - E(x))^2}\sqrt{\sum_{i=1}^{N}(y_i - E(y))^2}}. \end{cases} \tag{9}$$

Here, x and y denote the grayscale values of two adjacent pixels, and N refers to the total number of pixels. The original image correlation graphs for the three images are shown in Fig. 12(a). Note that adjacent pixels in the encrypted image Fig. 12(b) are completely randomly distributed, with significantly lower correlation.

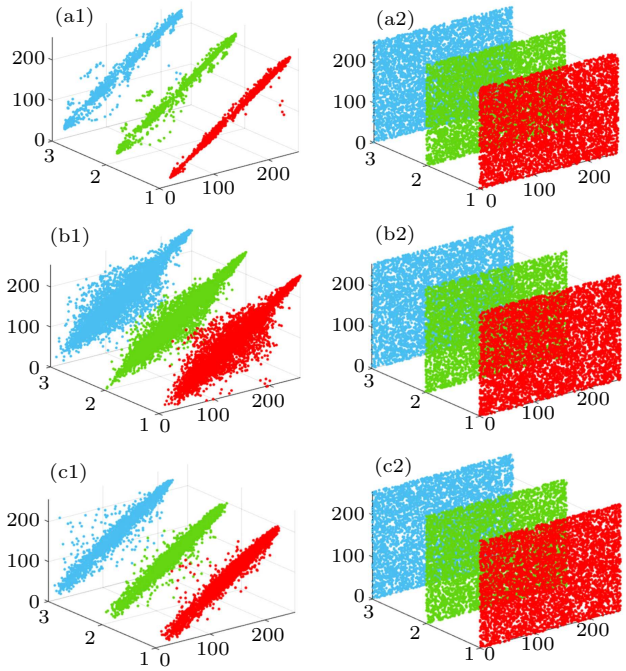


Fig. 12. Correlation tests. (a) Three directional correlations of the R channel in the plain images. (b) Three directional correlations of the R channel in the cipher images.

Table 5. Correlation coefficient results of plain and chiper images with information entropy.

Image	Channel	Plain image			Cipher image			
		Horizontal	Vertical	Diagonal	Horizontal	Vertical	Diagonal	Information entropy
4.2.01	R	0.9947	0.9934	0.9893	–0.0070	–0.0097	0.0093	7.9992
	G	0.9835	0.9831	0.9708	0.0031	0.0068	0.0058	7.9993
	B	0.9808	0.9818	0.9604	–0.0070	–0.0061	0.0006	7.9993
4.2.03	R	0.8618	0.9219	0.8523	–0.0021	–0.0067	0.0101	7.9992
	G	0.7660	0.8677	0.7391	–0.0051	0.0074	–0.0068	7.9992
	B	0.8883	0.9088	0.8417	–0.0021	0.0070	0.0132	7.9993
4.2.07	R	0.9648	0.9641	0.9558	–0.0012	0.0093	0.0063	7.9992
	G	0.9822	0.9809	0.9719	0.0023	0.0089	–0.0047	7.9993
	B	0.9696	0.9561	0.9405	0.0048	–0.0043	–0.0086	7.9994

Table 5 lists the calculated correlation coefficients and information entropy for images 4.2.01, 4.2.03, and 4.2.07 across three channels. The correlation between adjacent pixels in the original images is close to 1, while in the encrypted images it is close to 0, demonstrating that the encryption algorithm effectively breaks the connections between pixels. Furthermore, the calculated information entropy is close to the ideal value, indicating that the encryption method effectively scrambles the pixels.

(3) Key sensitivity analysis

Key sensitivity refers to the differences between the encrypted images obtained when the encryption key is slightly altered for the same original image. Common evaluation indicators include the number of pixel change rate (NPCR), the uniform average changing intensity (UACI), and the block average changing intensity (BACI).[45] Note that, the detailed mathematical expressions of NPCR and UACI indexes can be found in Ref. [46] and the BACI index is defined in Ref. [47]. This paper evaluates the sensitivity of the image encryption system through key sensitivity analysis. The initial value of the u_0 state variable of the memristor neural network (2) is set as the research object, and the change in each key group is 10^{-13}. Taking images 4.2.03 and 4.2.07 as examples, the three index values for the R, G, and B channels are calculated, respectively. The results and theoretical values of the indicators are listed in Table 6. It can be seen that the calculated results are close to the theoretical values, indicating that the encryption algorithm has a high key sensitivity and is difficult for attackers to crack.

Table 6. Key sensitivity analysis under different channels.

Image	Channel	NPCR (%)	UACI (%)	BACI (%)
4.2.03	R	99.6174	33.4532	26.7924
	G	99.6143	33.4827	26.7712
	B	99.5968	33.4378	26.7250
4.2.07	R	99.6155	33.4861	26.7785
	G	99.6059	33.4210	26.7646
	B	99.6184	33.4664	26.8172
Ideal values		99.6094	33.4635	26.7712

Table 7 shows the performance comparison results of the proposed algorithm and related studies in terms of NPCR, UACI, and BACI. The results show that the NPCR and UACI of the proposed algorithm are 99.6113% and 33.4578%, respectively, which are slightly better than the results in Refs. [48,49]. In addition, the BACI value of the proposed method is 26.7748%, which is higher than that of Refs. [42, 45]. This shows that the proposed algorithm has stronger random perturbation capability in bit-level diffusion. Comprehensive comparisons indicate that the proposed algorithm can achieve high diffusion and strong sensitivity at both the pixel and bit levels, and can effectively resist differential analysis and statistical attacks.

Table 7. Comparison of the NPCR, UACI, and BACI metrics.

Refs	NPCR	UACI	BACI
[40]	99.6119	33.4763	26.7845
[43]	99.6085	33.4748	26.7744
[44]	99.6148	33.4654	–
[45]	99.6275	33.5544	–
This work	99.6113	33.4578	26.7748

(4) Key space analysis

To resist exhaustive attacks on encrypted images, the algorithm must ensure a sufficiently large key space and strong security. It is generally believed that when the key space of the encryption scheme is higher than 2^{100}, the encryption scheme is secure and reliable and not easily cracked by exhaustive attacks. The proposed algorithm contains nine keys, namely, the six initial conditions of the hyperchaotic system (x_0, y_0, z_0, u_0, v_0, w_0) and the initial values of the three Logistic discrete chaotic sequences l_0, l_{01} and l_{02}. The precision of the nine secret keys is obtained by simulation, as shown in Table 8. The key space is calculated only by the precision difference between the keys, ignoring the range of initial values that can generate chaos. It can be obtained that the key space of the encryption scheme is $10^{148} \approx 2^{491}$, which is much higher than 2^{100}. Therefore, the encryption scheme is reliable and not easily attacked by exhaustive attacks.

Table 8. Key sensitivity with varying initial values.

Key	x_0	y_0	z_0	u_0	v_0	w_0	l_0	l_{01}	l_{02}
Errors	10^{-16}	10^{-18}	10^{-16}	10^{-17}	10^{-17}	10^{-17}	10^{-16}	10^{-15}	10^{-16}

(5) Plaintext attack analyses

The encryption algorithm often faces various security threats during communication and image transmission. Among them, known plaintext attack and chosen plaintext attack are particularly dangerous because attackers can infer the equivalent key or even recover the scrambling and diffusion matrices by using the known plaintext–ciphertext pairs or carefully selected input images. In traditional encryption algorithms, if the scrambling or diffusion process is not related to the characteristics of the plaintext, attackers may use statistical or differential analysis to reconstruct the internal mapping relationship. For the DNA-coding encryption algorithm proposed in this paper, the hyperchaotic sequences generated by IN-HNN are used to dynamically control the DNA encoding, decoding, and arithmetic operations of each sub-block. During the encryption process, the initial values of the chaotic system and the selection of the DNA encoding rules are all derived from the average gray level and differential energy of the plaintext image, achieving a strong coupling between the plaintext features and the chaotic sequence. In addition, the multi-round diffusion mechanism can ensure that even if only one pixel in the plaintext changes slightly, the ciphertext image will undergo a significant change. Therefore, the diffusion and chaotic generation of the algorithm are driven by the plaintext rather than relying on a fixed key, making the system highly sensitive to plaintext perturbations and thus capable of effectively resisting known plaintext attacks and chosen plaintext attacks.

(6) Noise attack test

In practical image transmission, ciphertexts are often exposed to noise disturbances, which may result in information degradation. An effective encryption scheme should be robust against such interference. To evaluate this property, 5%, 10%, and 20% salt-and-pepper noise were introduced into the ciphertext image. Using image 4.2.03 as an example, the corresponding encrypted and decrypted results are presented in Fig. 13. Although the added noise affects the ciphertext, the algorithm successfully recovers the plaintext, demonstrating strong robustness.

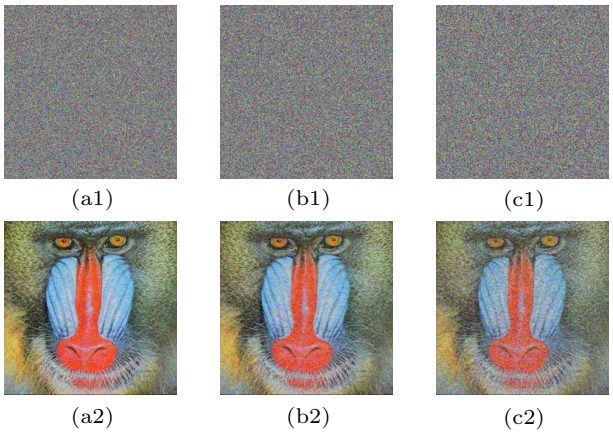


Fig. 13. Encrypted and decrypted images results under different noise levels: (a) 5% noise, (b) 10% noise, (c) 20% noise.

(7) Anti-shearing attack test

During image transmission, besides noise interference, cropping attacks can also lead to loss of image information. This study performed decryption on encrypted images after cropping $1/8$, $1/4$, and $1/2$ of original size. The cropped cipher image 4.2.03 and the corresponding decrypted image are shown in Fig. 14. It can be found that even with varying degrees of information loss, the decrypted images maintain a high degree of recovery, demonstrating that the proposed encryption algorithm effectively resists cropping attacks and exhibits strong robustness, thus providing strong support for information security.

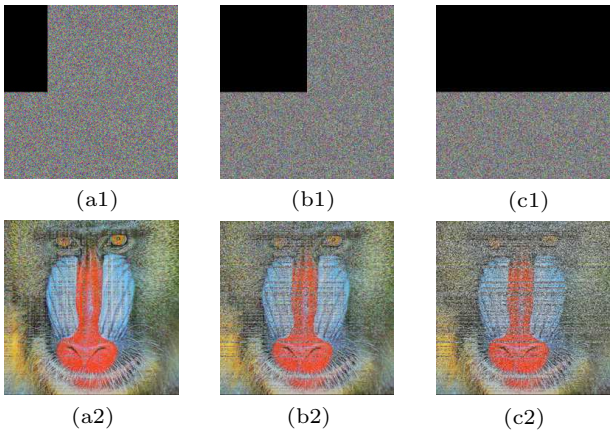


Fig. 14. Encrypted and decrypted results under cropping attacks with different ratios: (a) $1/8$ ratio, (b) $1/4$ ratio, (c) $1/2$ ratio.

6. Conclusion

This paper proposed a memristor synapse-coupled IN-HNN network model, which can exhibit rich dynamical behaviors. By introducing a simple ReLU function, a new memristor system model was established first, which can serve as an effective connection coupler for the neural synapse. Then the memristive neuronal network was presented. Numerical analysis results showed that the system dynamics were highly sensitive to the memristor coupling strength, self-connection weight, and inter-connection weight, and can exhibit significant hyperchaotic characteristics. Also, the initial-induced multi-stable coexistence phenomena were confirmed. Circuit simulations further verified the correctness of the IN-HNN coupled system. In the final, at the application level, an image encryption scheme on account of DNA encoding and the hyperchaotic sequence was proposed. Test results showed that the encryption algorithm exhibited good robustness in resisting statistical attacks, differential attacks, and noise interference, and can effectively defend against plaintext attacks. Notice that, the new approach for the modeling and implementation of large-scale brain-like neural networks will be developed in the future.

Acknowledgements

Project supported by the Training Plan of Young Backbone Teachers in Universities of Henan Province (Grant No. 2023GGJS142), the Key Scientific Research of Colleges and Universities in Henan Province, China (Grant No. 25A120009), Changzhou Leading Innovative Talent Introduction and Cultivation Project (Grant No. CQ20240102), and Changzhou Applied Basic Research Program (Grant No. CJ20253065).

References

[1] Ma J 2023 *J. Zhejiang Univ-Sc. A* **24** 109
[2] Zhou X H, Sun K H, Wang H H and Yao Z 2024 *Nonlinear Dyn.* **112** 9547
[3] Ma Q Q, Lu A J and Huang Z 2024 *Chin. Phys. B* **33** 120502
[4] Min F, Chen C and Broderick N G R 2025 *IEEE Trans. Neur. Net. Lear.* **36** 11632
[5] Babcock K L and Westervelt R M 1986 *Physica D* **23** 464
[6] Wheeler D W and Schieve W C 1997 *Physica D* **105** 267
[7] Zhao S, Chuah J H, Khairuddin A S M, Zhang Y Z and Chen C J 2025 *Int. J. Bifurcation Chaos* **35** 2530001
[8] Zhao S, Chuah J H, Khairuddin A S M and Chen C J 2024 *Phys. Scr.* **100** 015229
[9] Song Z G, Zhen B and Hu D 2020 *Cogn. Neurodyn.* **14** 359
[10] Song Z G, Xu J and Zhen B 2019 *Math. Biosci. Eng.* **16** 6406
[11] Boya B F B, Ramakrishnan B, Effa J Y, Kengne J and Rajagopal K 2022 *Physica A* **602** 127458
[12] Sriram S, Danao A A, Fonzin T F, Rajagopal K and Kengne J 2022 *Phys. Scr.* **97** 125207
[13] Liu P, Yong J, Sun J, Wang Y and Zhao J 2024 *Neural Comput. Applic.* **36** 13293
[14] Priyanka T M C, Vignesh D, Gowrisankar A and Ma J 2025 *Eur. Phys. J. Plus* **140** 363
[15] Yu F, Su D, He S, Wu Y, Zhang S and Yin H 2025 *Chin. Phys. B* **34** 050502
[16] Lai Q, Yang L and Chen G 2025 *IEEE Trans. Ind. Electron.* **72** 969
[17] Lai Q and Liu Y 2025 *Sci. China Technol. Sc.* **68** 1320401
[18] Peng Y, Lan Z, Sun K and Xu W 2023 *Opt. Laser Technol.* **165** 109543
[19] Li X, He Q, Yu T, Cai Z and Xu G 2024 *Chin. Phys. B* **33** 030505
[20] Zhang S, He D, Li Y, Lu D and Li C B 2025 *IEEE Trans. Autom. Sci. Eng.* **22** 17828
[21] Huang L, Wang S, Lei T, Huang K and Li C 2024 *Int. J. Bifurcation Chaos* **34** 2450022
[22] Biamou A L M, Tamba V K, Kuate G C G, Takougang A C N and Fotsin H B 2023 *Phys. Scr.* **99** 015215
[23] Sun J, Ma Y, Wang Z and Wang Y 2023 *Nonlinear Dyn.* **111** 8751
[24] Wang X, Du J R, Li Z J, Ma M L and Li C L 2024 *Acta Phys. Sin.* **73** 110503 (in Chinese)
[25] Li C L, Wang S D, Li H M, Li Z J, Liu L Z and Qian K 2026 *Chaos Solit. Fract.* **202** 117457
[26] Lai Q and Hua H 2025 *Expert Syst. Appl.* **264** 125854
[27] Zhang S, Chen C, Zhang Y, Cai J, Wang X and Zeng Z 2025 *IEEE Trans. Syst. Man Cy. A* **55** 735
[28] Lai Q, Liu Y and Fortuna Y 2024 *IEEE Trans. Circuits Syst. I* **71** 4665
[29] Zhao S, Chuah J H, Khairuddin A S M and Chen C 2024 *Phys. Scr.* **100** 015229
[30] Chen C, Min F, Hu F, Cai J and Zhang Y 2023 *Chaos Solit. Fract.* **173** 113727
[31] Meng F Q and Wu G 2024 *Expert Syst. Appl.* **254** 124413
[32] Zhou L L, Lin Z, Tan F and Chen P 2025 *Expert Syst. Appl.* **281** 127475
[33] Zhou L L, Chen Q, Tan F and Wu C 2026 *Expert Syst. Appl.* **297** 129272
[34] Deng Q, Wang C and Lin H 2024 *Chaos Solit. Fract.* **178** 114387
[35] Shi F, Xu X, Chen J, Banerjee S and Mou J 2025 *Nonlinear Dyn.* **113** 26753
[36] Chen C J, Bao H, Zhang Y, Yu Y, Zhao S, Yang Y and Chen L Y 2025 *IEEE Trans. Circuits Syst. I* **72** 4854
[37] Min F, Zhai G, Yin S and Zhong J 2024 *Nonlinear Dyn.* **112** 5687
[38] Xu Q, Chen X, Wu H, Lu H H C, Parastesh F and Wang N 2024 *IEEE Trans. Circuits Syst. II* **71** 4551
[39] Chen X, Wang N, Wang K, Chen M, Parastesh F and Xu Q 2024 *Nonlinear Dyn.* **112** 20365
[40] Chen C J and Min F H 2022 *Eur. Phys. J. Spec. Top.* **231** 2979
[41] Li C, Zhang Y, Li H and Zhou Y 2024 *Vis. Comput.* **40** 731
[42] Chen C, Gao B, Yu Y, Zhao S, Yang Y, Chen L and Bao H 2025 *Chaos Solit. Fract.* **199** 116871
[43] Das S and Sanyal M K 2023 *Int. J. Inf. Technol.* **15** 1015
[44] Wang C, Chong Z, Zhang H, Ma P and Dong W 2024 *Integration* **96** 102138
[45] Zhang Y 2025 *Math. Comput. Simul.* **232** 382
[46] Zhou Y, Li C L, Li W, Li H M, Feng W and Qian K 2021 *Nonlinear Dyn.* **103** 2043
[47] Zhang Y 2021 *Inf. Sci.* **550** 313
[48] Gao X, Sun B, Cao Y, Banerjee S and Mou J 2023 *Chin. Phys. B* **32** 030501
[49] Li X, He Q, Yu T, Cai Z and Xu G 2024 *Chin. Phys. B* **33** 030505